

Learn-Morph-Infer: a new way of solving the inverse problem for brain tumor modeling

Ivan Ezhov^{1,2}, Kevin Scibilia¹, Katharina Franitza³, Felix Steinbauer¹, Suprosanna Shit^{1,2}, Lucas Zimmer⁴, Jana Lipkova^{5,6,7}, Florian Kofler^{1,2,9}, Johannes Paetzold^{1,2}, Luca Canalini⁸, Diana Waldmannstetter¹, Martin Menten^{1,2}, Marie Metz^{2,9}, Benedikt Wiestler^{2,9}[‡], and Bjoern Menze⁴[‡]

¹*Department of Informatics, TUM, Munich, Germany*

²*TranslaTUM - Central Institute for Translational Cancer Research, TUM, Munich, Germany*

³*Department of Mechanical Engineering, TUM, Munich, Germany*

⁴*Department of Quantitative Biomedicine of UZH, Zurich, Switzerland*

⁵*Department of Pathology, Brigham and Women's Hospital, Harvard Medical School, Boston, MA*

⁶*Broad Institute of Harvard and MIT, Cambridge, MA*

⁷*Data Science Program, Dana-Farber Cancer Institute, Boston, MA*

⁸*Fraunhofer MEVIS, Bremen, Germany*

⁹*Neuroradiology Department of Klinikum Rechts der Isar, TUM, Munich, Germany*

[‡] *Contributed equally as senior authors*

Code: <https://github.com/IvanEz/learn-morph-infer>

***Correspondence:**

Ivan Ezhov

ivan.ezhov@tum.de

Abstract

Current treatment planning of patients diagnosed with brain tumor could significantly benefit by accessing the spatial distribution of tumor cell concentration. Existing diagnostic modalities, such as magnetic-resonance imaging (MRI), contrast sufficiently well areas of high cell density. However, they do not portray areas of low concentration, which can often serve as a source for the secondary appearance of the tumor after treatment. Numerical simulations of tumor growth could complement imaging information by providing estimates of full spatial distributions of tumor cells. Over recent years a corpus of literature on medical image-based tumor modeling was published. It includes different mathematical formalisms describing the forward tumor growth model. Alongside, various parametric inference schemes were developed to perform an efficient tumor model personalization, i.e. solving the inverse problem. However, the unifying drawback of all existing approaches is the time complexity of the model personalization that prohibits a potential integration of the modeling into clinical settings. In this work, we introduce a methodology for inferring patient-specific spatial distribution of brain tumor from T1Gd and FLAIR MRI medical scans. Coined as *Learn-Morph-Infer* the method achieves real-time performance in the order of minutes on widely available hardware and the compute time is stable across tumor models of different complexity, such as reaction-diffusion and reaction-advection-diffusion models. We believe the proposed inverse solution approach not only bridges the way for clinical translation of brain tumor personalization but can also be adopted to other scientific and engineering domains.

1 Introduction

Glioblastoma (GBM) is the most aggressive brain tumor, characterized by varying and unknown infiltration into the surrounding tissue. After resection of the tumor mass visible in MRI scans, current treatment includes radiotherapy targeting tissue around the visible lesion to account for residual tumor cells. Tumor recurrence is present in most cases, possibly due to patient-specific and non-uniform distribution of residual tumor cells. Personalization of the clinical (irradiation) target volume, could spare more healthy tissue and increase progression-free survival by potentially avoiding recurrence¹⁻⁴.

Current computational approaches for personalizing radiotherapy planning often rely on solving an inverse problem for GBM growth models⁴⁻¹³. In this context, the growth (forward) models are based on partial differential equations (PDEs) that describe the evolution of tumor cell density in the brain anatomy. The inverse model aims to identify free parameters of the forward model that best match the observation, e.g. tumor outlines from medical imaging modalities. To identify such parameters the inverse problem can be cast as constrained optimization^{5, 14, 15} or Bayesian inference formulations^{4, 16, 17}.

Predominantly, existing forward GBM models view tumor progression at macroscopic level by describing gross bio-mechanical phenomena. These include diffusive motion and proliferation of tumor cells (under simplistic reaction-diffusion PDEs)⁸, interaction between the tumor and surrounding tissue (i.e. mass-effect)¹¹, necrotic core formation¹⁸, etc. Despite methodological advances in computing the inverse model, the total time for model personalization is still large amounting to multiple hours using such simplistic forward models^{11, 15, 19}. For example, in Scheufele et al.¹⁵ the authors exploit highly efficient quasi-Newton optimisation scheme to infer parameters of the reaction-diffusion model. The inference converges after ~ 5 hours of compute on 11 dual-x86 CPU nodes for 256^3 resolution. In Subramanian et al.¹¹, the mass-effect model is solved using analogous optimisation scheme but implemented on GPU leading to the same order of compute time for the 256^3 grid (and up to 1 hour for 128^3 resolution). Bayesian methods providing uncertainty estimate of the parametric inference⁴ can take even longer time (up to days) of compute on specialized CPU clusters. Few recent machine learning approaches^{16, 20} aim to speed-up the inference by leveraging access to large simulated data. However, Ezhov et al.¹⁶ still requires vast amount of forward model evaluations for convergence of parametric estimation under Bayesian settings for each new patient. In turn, Pati et al.²⁰ requires access to a dataset of inferred model parameters that can become prohibitively expensive to collect with growing complexity of the growth tumor model.

A potential integration of brain tumor modeling into clinical practice would require access to a large cohort of longitudinal clinical data, allowing to estimate the clinical value of a patient outcome's forecast by the tumor models²¹. Integration of current macroscopic models would also require a thorough analysis of forecast

consistency between the macroscopic description and higher complexity microscopic models encompassing subcellular biophysics. For this it is paramount to bring the computational cost of the inverse modeling to reasonable time. Here, we propose a neural network based methodology for predicting a patient-specific spatial distribution of GBM (from a single time-point medical scans, namely T1Gd and FLAIR MRI) that does not require neither sampling nor optimization. The method achieves lightning-fast performance in the order of minutes on widely available hardware and the compute time is stable across tumor models of different complexity. This in turn opens the possibility of rapid testing various biophysical models on a large dataset of patients and hence bridging the way for clinical translation.

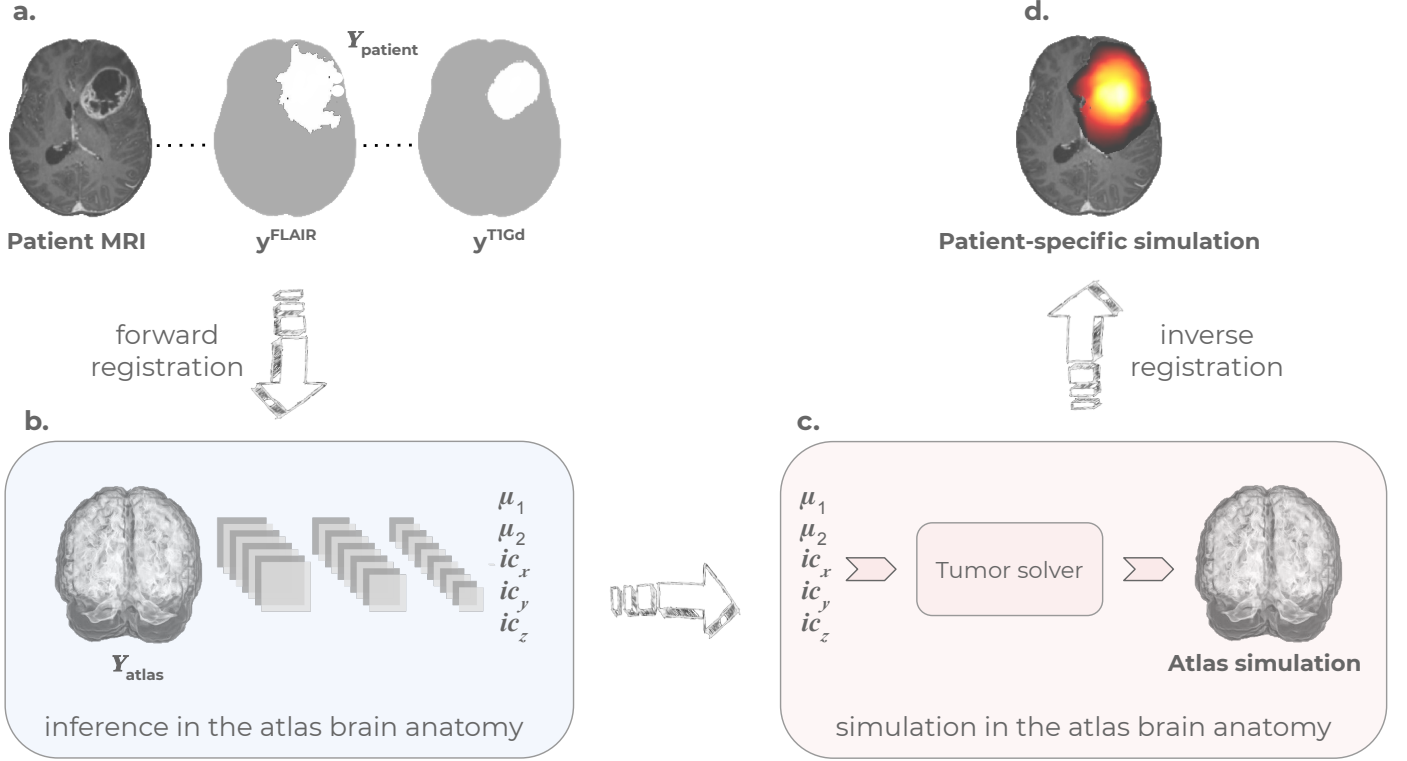


Figure 1: A sketch of the inference procedure of the *Learn-Morph-Infer* pipeline. First, patient’s brain tumor segmentations $\{y^{T1Gd}, y^{FLAIR}\}$ are morphed to the brain atlas space (a). A trained on synthetic data network inputs the morphed segmentations and outputs corresponding tumor model parameters $\{\mu_1, \mu_2, ic_x, ic_y, ic_z\}$ (b). The inferred parameters are used to simulate a tumor in the atlas space (c). Finally, the simulated tumor is morphed back to the patient space (d).

2 Method

2.0.1 Learn-Morph-Infer Pipeline

To solve the inverse problem we rely on single time-point MRI observations of a tumor $Y = \{y^{T1Gd}, y^{FLAIR}\}$. Given a tumor observation Y , our goal is to calibrate a set of personalized parameters θ_c of the forward tumor growth model that infers the underlying patient-specific tumor cell density $c_{patient}$ in the patient anatomy. For a given patient, this is achieved via the proposed *Learn-Morph-Infer* pipeline:

- We register a patient MRI image to the brain atlas ²² and obtain a transformation matrix.
- The transformation matrix is used to morph scans based on the patient anatomy $Y_{patient}$ to scans in the atlas anatomy Y_{atlas} as illustrated in Fig. 1a-b.
- A neural network, that has learned to solve the inverse problem $Y_{atlas} \rightarrow \theta_c$ through prior training on simulated data Y_{sim} (Fig. 1), predicts θ_c during inference time, Fig. 1b.
- These parameters θ_c are used as input in the tumor growth model (forward solver) to infer a tumor cell density c_{atlas} in the atlas space, Fig. 1c.
- The tumor volume c_{atlas} is transformed back to the patient space with the inverse transformation matrix, yielding $c_{patient}$ as displayed in Fig. 1d.

2.0.2 Forward tumor model

We aim to solve the inverse problem in the context of brain tumor modeling. We probe independently two types of non-linear PDEs:

Reaction-diffusion equation. First, we consider the Fisher-Kolmogorov PDE describing the evolution of the tumor cell concentration c by considering cell diffusion and proliferation,

$$\frac{\partial c}{\partial t} = \nabla \cdot (\mathbf{D} \nabla c) + \rho c(1 - c) \quad (1)$$

$$\nabla c \cdot \mathbf{n} = 0 \quad \text{boundary condition} \quad (2)$$

Here, ρ denotes the tumor proliferation rate while the infiltrative behaviour of the tumor is modelled by the diffusion tensor $\mathbf{D} = D \cdot \mathbb{I}$ ⁸. The equation is solved in a three dimensional atlas brain anatomy segmented into white matter (WM), grey matter (GM) and cerebrospinal fluid (CSF). The diffusion coefficient D is computed for each voxel \mathbf{i} with location (i_x, i_y, i_z) as $D_i = p_{w_i} D_w + p_{g_i} D_g$, where p_w, p_g describe percentages and D_w, D_g diffusion coefficients of WM and GM respectively. In our model, a relation $D_w = 10 \cdot D_g$ is assumed, similarly to ⁴. No cell diffusion into CSF is feasible according to the model. The solver based on this growth model takes $\theta_c = \{D_w, \rho, T, i_{c_x}, i_{c_y}, i_{c_z}\}$ as input and returns a tumor cell density c . The parameters $\mathbf{x} = (i_{c_x}, i_{c_y}, i_{c_z})$

define the initial condition where the tumor is initialized at time $t=0$. Tumor is simulated until the time of detection T .

Reaction-diffusion-advection equation. The second type is a non-linear reaction-diffusion-advection PDE analogous to ¹¹. In the following, the brain tissue will be represented by $\mathbf{m} = (m_{WM}(\mathbf{i}, t), m_{GM}(\mathbf{i}, t), m_{CSF}(\mathbf{i}, t))$ for each voxel \mathbf{i} and time t . The normalized tumor cell density $c = c(\mathbf{i}, t)$ can be modelled by the following equations:

$$\frac{\partial c}{\partial t} = \nabla \cdot (\mathbf{D} \nabla c) - \nabla(c\mathbf{v}) + \rho c(1 - c) \quad (3)$$

$$\frac{\partial \mathbf{m}}{\partial t} + \nabla \cdot (\mathbf{m} \otimes \mathbf{v}) = 0 \quad (4)$$

$$\nabla \cdot (\lambda \nabla \mathbf{u} + \mu(\nabla \mathbf{u} + \nabla \mathbf{u}^\top)) = \gamma \nabla c \quad (5)$$

$$\frac{\partial \mathbf{u}}{\partial t} = \mathbf{v} \quad (6)$$

$$\nabla c \cdot \mathbf{n} = 0 \quad \text{boundary condition} \quad (7)$$

$$\mathbf{m} = 0 \quad \text{boundary condition} \quad (8)$$

$$\mathbf{u} = 0 \quad \text{boundary condition} \quad (9)$$

$$\mathbf{v} = 0 \quad \text{boundary condition} \quad (10)$$

Coupling the Eqn. 3 to a linear elasticity model Eqn. 5 allows considering deformation in the anatomy due to a mass effect induced by tumor growth²³. The linear elasticity model is defined by the Lamè coefficients λ and μ as specified in Eqn. 5. The displacement \mathbf{u} is respresented in the advection term of Eqn. 3. The degree of the mass effect depends on the selection of the mass effect parameter γ . Choosing $\gamma=0$ would result in the simplistic reaction-diffusion PDE with $\mathbf{u}=0$ and $\mathbf{v}=0$.

2.0.3 Linking cell density with MRI signal

MRI modalities capture structural information about the brain tumor. T1Gd contrasts the tumor core, whereas FLAIR informs about the area of the edema in addition to the tumor core. It is established practice^{4,11,24,25} to consider binary segmentations corresponding to the MRI scans to inform biophysical models. The binary masks contain zeros in the area of healthy tissues, and are non-zero in the tumor related area. In order to relate the segmentations $D = \{\mathbf{y}^{T1Gd}, \mathbf{y}^{FLAIR}\}$ to a simulated tumor cell density c , we threshold the density at randomly sampled levels c_t^{T1Gd} and c_t^{FLAIR} ($c_t^{T1Gd} > c_t^{FLAIR}$) to obtain $D_{sim} = \{\mathbf{y}_{sim}^{T1Gd}, \mathbf{y}_{sim}^{FLAIR}\}$ reproducing the real segmentations.

2.0.4 Learning the inverse model in atlas space

As discussed in the previous section, the key step of the *Learn-Morph-Infer* pipeline is to learn the inverse tumor model using a neural network that can infer a set of personalized parameters θ_c from corresponding tumor observations Y_{atlas} . In order to create a dataset for the network training, we generate 100,000 tumors in the atlas space by randomly sampling tumor model parameters $\{D_w, \rho, T, ic_x, ic_y, ic_z, c_t^{T1Gd}, c_t^{FLAIR}\}$ within physiologically plausible ranges²⁶. To form the neural network input, the simulated MRI segmentations are combined into one volume $\mathbf{y}_{sim}^{MRI} = \mathbf{y}_{sim}^{T1Gd} + \mathbf{y}_{sim}^{FLAIR}$, similar to Ezhov et al.¹⁷.

Now, the question is what should be used as a network prediction? It is tempting to try to predict the tumor model parameters directly. However, it is well known that the inverse problem is highly ill-posed, i.e. numerous sets of dynamic parameters $\{D_w, \rho, T\}$ correspond to the same simulated cell density profile. Thus, we have two sources of prediction error: a) coming from the fact that we learn a mapping from one to many. Imagine we have two sets of dynamic parameters $\{D_w, \rho, T\}$ and $\{D_w^*, \rho^*, T^*\}$ that result in the same tumor profile \mathbf{y}_{sim}^{MRI} . If we train a network in a supervised fashion, everytime the network predicts $\{D_w^*, \rho^*, T^*\}$ for $\{D_w, \rho, T\}$ - \mathbf{y}_{sim}^{MRI} pair (and vice-versa), it will be falsely penalized; b) the actual error that comes from limited network capacity to accurately learn the mapping.

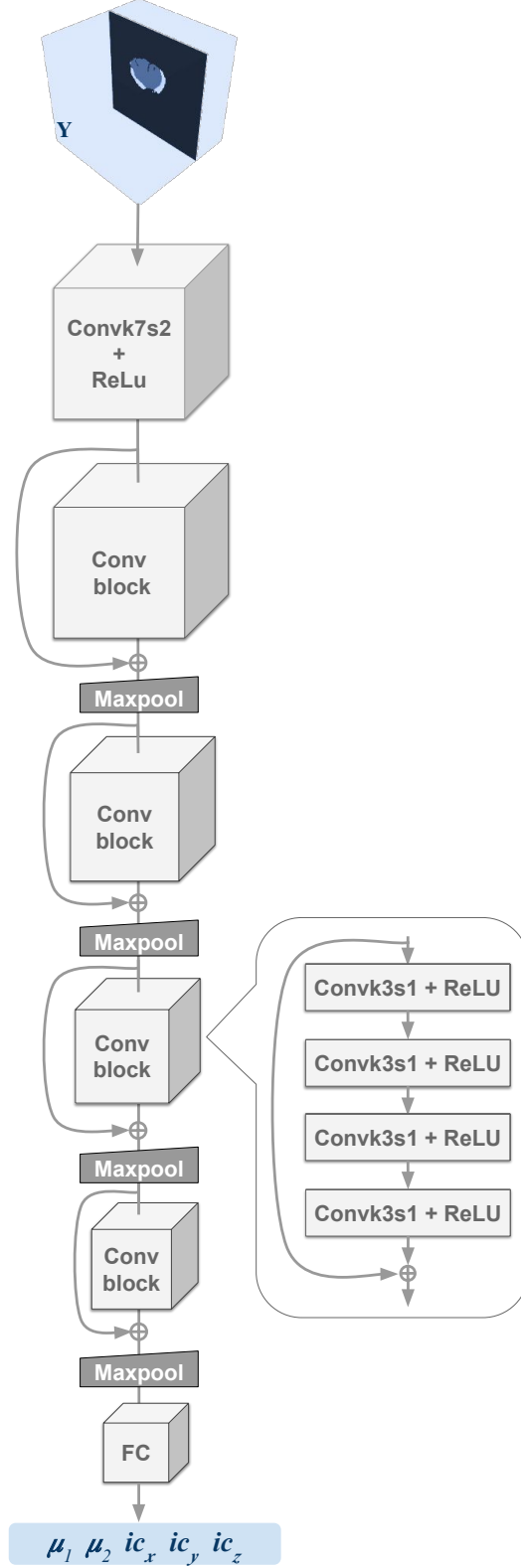


Figure 2: A design of the inverse model network - one of the key elements of the *Learn-Morph-Infer* pipeline. The network design represents a ResNet type architecture. It takes as an input the binary brain tumor segmentations $\{\mathbf{y}^{T1Gd}, \mathbf{y}^{FLAIR}\}$ and outputs $\{\mu_1, \mu_2, ic_x, ic_y, ic_z\}$.

Clearly, the error of type (a) should negatively affect the learning performance, as the network may be

penalized for making a sensible prediction. To circumvent this we do not predict the parameters directly. As evident from Eqn. 1, normalization of the time parameter T in Eqn. 1 is equivalent to re-scaling of the proliferation ρ and diffusion D coefficients²⁷. This means that for sets $\{D_w, \rho, T\}$ and $\{D_w^*, \rho^*, T^*\}$ corresponding to the same simulated tumor, combinations of time-independent parameters $\mu_1 = \sqrt{D_w T}$, $\mu_2 = \sqrt{T \rho}$ stay constant ($\sqrt{D_w T} = \sqrt{D_w^* T^*}$, $\sqrt{T \rho} = \sqrt{T^* \rho^*}$). Hence, predicting these combinations of time-independent parameters μ_1 and μ_2 relaxes the error type (a). In order to calculate back the $\{D_w, \rho, T\}$, we introduce a third combination as $v = 2\sqrt{D_w \rho}$. As it is not possible to infer the velocity v from a single time-point observation, we set the velocity equal to mean velocity of the used sampling range, 200 mm/year (note also that for our purpose the choice of v is irrelevant as any tumor simulation can be obtained with arbitrary v ⁸). Given $\{\mu_1, \mu_2, v\}$, we can calculate $\{D_w = \frac{\mu_1 v}{2\mu_2}, \rho = \frac{\mu_2 v}{2\mu_1}, T = \frac{2\mu_2 \mu_1}{v}\}$.

Following this reasoning we make the network to predict five parameters $\{\mu_1, \mu_2, i_{c_x}, i_{c_y}, i_{c_z}\}$. Note that we do not predict $\{c_t^{t1Gd}, c_t^{FLAIR}\}$ as we do not need the threshold parameters at further steps of the *Learn-Morph-Infer* pipeline.

The network design. The network we choose to learn the inverse model represents a convolutional architecture, depicted in Fig. 2. Every convolution in the network is followed by a rectified linear unit (ReLU) nonlinearity. The input is passed through an initial convolution of kernel size 7, stride 2 and 64 filters (k7s2f64), downsampling the volume to 64^3 and increasing the number of channels to 64. This volume of size $64^3 \times 64$ is input through four convolutional blocks, where every convolutional block contains four convolutions of kernel size 3, stride 1 and 64 filters (i.e. number of filters is kept constant throughout the network). A convolutional block uses a skip connection to learn a residual mapping²⁸, with the input being added element-wise to the output of the four convolutions. The first three convolutional blocks are followed by a MaxPool3D layer (with parameters k2s2) to downsample the 3D volumes by two. The last convolutional block is followed by a global average pooling layer, shrinking the 64 3D volumes to 64 neurons that can be linked through a fully connected (FC) layer to the output. These outputs are linearly interpolated into the $[-1, 1]$ range for training.

As seen from our experiments below, the best performance was achieved by using two separate architecturally identical networks predicting the parameters $\{\mu_1, \mu_2\}$ and the initial location $\{i_{c_x}, i_{c_y}, i_{c_z}\}$, respectively.

3 Results

Data and implementation details The simulated tumors used for training the network have resolution of 128^3 . The simulations were generated by randomly sampling patient-specific parameters from the following ranges: $D_w \in [0.0002 \frac{\text{cm}^2}{\text{d}}, 0.015 \frac{\text{cm}^2}{\text{d}}]$, $\rho \in [0.002 \frac{1}{\text{d}}, 0.2 \frac{1}{\text{d}}]$, $T \in [50\text{d}, 150\text{d}]$, $x \in [0.15, 0.7]$, $y \in [0.2, 0.8]$, $z \in [0.15, 0.7]$, $c^{t1Gd} \in [0.5, 0.85]$, $c^{FLAIR} \in [0.05, 0.5]$. The elasticity model parameters λ, μ, γ were taken

from ²³. Tumors that are unrealistically small or large have been discarded (based on minimum and maximum tumor sizes of real tumors from BraTS dataset ²⁹). The simulations dataset is then divided into a training set (80000 tumors), validation set (8000 tumors) and test set (12000 tumors).

The network is initialized with He initialization as in the original ResNet architecture²⁸, and is trained with the AdamW³⁰ optimizer, which is a variant of the Adam optimizer³¹ using decoupled weight decay. We use an initial learning rate of 6×10^{-5} which is decayed exponentially after every batch by a factor of 0.999997. Weight decay with a factor of 0.05 is used as regularization technique. Furthermore, we train the network with a batch size of 32 and the Mean Squared Error (MSE) loss function. All training and testing runs were executed on an NVIDIA Quadro RTX 6000 with the PyTorch framework.

For the registration between the patient and atlas brain MRI scans, we use the Advanced Normalization Tools (ANTs)³². We choose a deformable SyN registration that ensures providing both forward and inverse transformation with step-size 0.25, weight 1, region radius for cross correlation computation $r=4$. The cross-correlation is used as a similarity metric. The optimization is performed over two resolutions with a maximum of 50 iterations at the coarsest level, and 20 at the final level. The tumor area on the patient scan was masked for the registration. We use a Gaussian regularizer with a sigma of 3 operating on the similarity gradient. These settings provided high morphing quality at relatively fast compute (~ 2 minutes).

Experiments We perform two sets of experiments: a) on synthetic data to estimate accuracy of the learnable inverse model, and b) on patient MRI scans to qualitatively probe transferability of the method to real data.

Experiment			MAE		
ID	Tumor Model	Predicted Parameters	GM	WM	CSF
1	<i>FK</i>	$\{D_w, \rho, T\}, \{\mathbf{x}\}$	0.461	0.463	0.0
2		$\{\mu_1, \mu_2\}, \{\mathbf{x}\}$	0.059	0.059	0.0
3		$\{\mu_1, \mu_2, \mathbf{x}\}$	0.057	0.057	0.0
4	<i>ME</i>	$\{D_w, \rho, T\}, \{\mathbf{x}\}$	0.089	0.087	0.059
5		$\{\mu_1, \mu_2\}, \{\mathbf{x}\}$	0.059	0.057	0.054
6		$\{\mu_1, \mu_2, \mathbf{x}\}$	0.055	0.054	0.054

Table 1: Ablation analysis on the test set (12k samples). In total we perform 6 experiments. First three experiments are performed for the Fisher-Kolmogorov (FK) tumor model: 1) Two separate neural networks predicting $\{D_w, \rho, T\}$ and $\{\mathbf{x} = (ic_x, ic_y, ic_z)\}$, 2) Two separate neural networks for prediction of the growth $\{\mu_1, \mu_2\}$ and location $\{\mathbf{x}\}$ parameters, 3) Single neural network predicting $\{\mu_1, \mu_2, \mathbf{x}\}$. The last experiments 4-6 are analogous but performed for the mass-effect (ME) model. Mean absolute error (MAE) $\|c_{sim} - c_{gt}\|$ in white and gray matter for the simulated tumor cell densities thresholded at different c_t is used for all experiments. For both FK and ME models the usage of single network predicting time-independent parameters results in a notable increase in accuracy compared to the time-dependent counterpart.

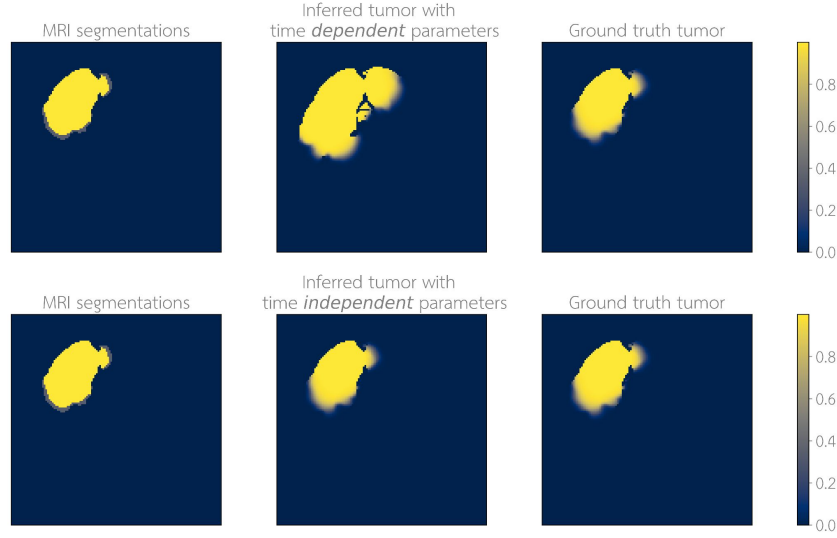


Figure 3: Qualitative comparison between the tumors inferred using the *Learn-Morph-Infer* pipeline with two different network training strategies: with time dependent (D_w, ρ, T, \mathbf{x}) parameters as network output, and time-independent (μ_1, μ_2, \mathbf{x}) parameters as output. The examples correspond to the Fisher-Kolmogorov tumor model with MAE equal 0.495 (within WM) and 0.496 (within GM) for time dependent inference, and 0.048 (within WM) and 0.048 (within GM) for time independent inference.

Synthetic test To perform sensitivity analysis, we tested the proposed *Learn-Morph-Infer* pipeline on simulated data for which we know the ground truth. We form synthetic data by thresholding a simulated tumor c_{gt} at two levels (analogously to how we created the training data). Then we pass the obtained thresholded volumes through the pipeline to infer tumor cell distribution c_{pred} . Finally we quantitatively compare the difference between c_{gt} and c_{pred} .

In Tab.1, for two different tumor models we show results of the ablation analysis, wherein we perform multiple experiments varying the neural network input and output configurations. First, we provide empirical proof that a network predicting D_w, ρ, T instead of time-independent parameter combinations μ_1, μ_2 cannot be trained reliably. Mean absolute error drops significantly when the network predicts D_w, ρ, T combination. Second, we tested whether the performance can be improved by learning two separate networks predicting growth $\{\mu_1, \mu_2\}$ and initial location parameters $\{\mathbf{x} = (ic_x, ic_y, ic_z)\}$, respectively. This test did not reveal an improvement compared to a single network predicting all parameters. Analogous experiments were performed for the mass-effect tumor model.

The Fig. 3 qualitatively showcases the accuracy of inference using the *Learn-Morph-Infer* pipeline. As discussed before, depending on the network training strategy (either predicting time dependent D_w, ρ, T, \mathbf{x} parameters, or time-independent μ_1, μ_2, \mathbf{x} parameters as network output), the accuracy of final simulated tumor notably differs. If the proposed learning with time independent combinations of parameters (resulting in MAE of the order 0.05) provides quite close to the ground truth tumor profile, than the learning with time dependent

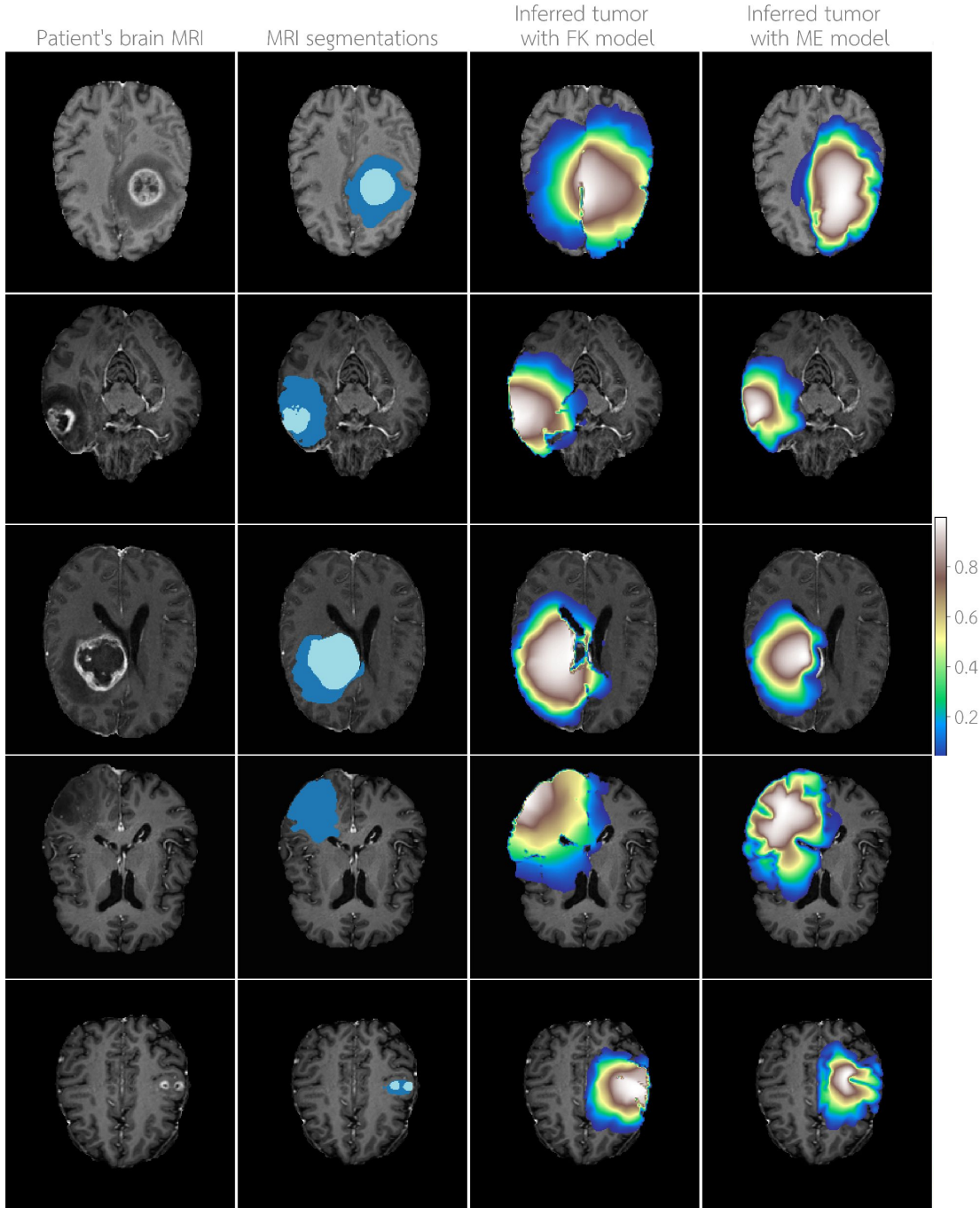


Figure 4: Examples of patient-specific simulations produced using the *Learn-Morph-Infer* method. The inverse model network was trained on samples from the Fisher-Kolmogorov (3rd column) and mass effect (4th column) forward models.

combinations (with MAE of the order 0.5) makes the inference hardly useful.

Real MRI patient data We performed validation of the method on a large cohort (80) of brain tumor patients which underwent MRI testing. Binary segmentation corresponding to the T1Gd and FLAIR modalities were used as input to the *Learn-Morph-Infer* method. Fig. 4 showcases qualitative examples of inferred tumor simulations for various tumor grades and locations in patients brain. Based on these results we observe generalization of the inverse model network (trained on synthetic data) to real MRI segmentations.

Computing time The total time including registration, morphing to atlas space, inference, tumor simulation, and morphing back to patient space is 4-7 minutes. The inference time for inverse model network’s inference is around 2 seconds for 128^3 resolution. Crucially, the inference time for the more complicated model with mass effect stays the same as for the Fisher-Kolmogorov tumor model. This emphasizes the key practical contribution of the proposed method in that it allows constant time model personalization for an arbitrary tumor model complexity.

4 Conclusion

We present a learnable brain tumor model personalization methodology. We demonstrate that it is feasible to learn an inverse model in a supervised fashion from a data set of numerical simulations. We show that the choice of output can crucially affect network’s performance - predicting time-independent combinations of parameters notably outperforms time-dependent counterparts. Such time-independent parametrization is not limited to the PDEs considered here, and thus the proposed *Learn-Morph-Infer* pipeline can be adopted to other inverse problems in natural science and engineering disciplines. For the brain tumor growth model, the *Learn-Morph-Infer* pipeline provides real-time performance of the parametric inference. Most importantly, the personalization time is stable across tumor models of different numerical complexity. These performance benefits pave the way for clinical testing of various mathematical tumor descriptions on a large cohort of patients.

Data Availability

All requests for the data used in the study will be reviewed by the authors and processed in accordance with institutional guidelines.

Code Availability

The code is implemented in PyTorch, and is available at github.com/IvanEz/learn-morph-infer. The code is provided under the GNU free software license.

Author Contributions

I.E. and K.S. conceived and designed the study. I.E., K.S., K.F., F.S., L.Z. performed the experiments. M.M., J.L., B.W. curated the dataset. I.E., S.S., F.K., J.P. analyzed the results. L.C., D.W. curated the image registration part of the pipeline. I.E., K.F., K.S., M.M., B.M. prepared the manuscript. B.W. and B.M. supervised the study.

Competing Interests

The authors declare that they have no competing financial interests.

Ethics Oversight

Institutional and ethical approval was obtained from our Institutional Review Board (protocol 202/19 S), and written informed consent was waived for this retrospective analysis.

References

1. Stupp, R., Brada, M., Van Den Bent, M., Tonn, J.-C. & Pentheroudakis, G. High-grade glioma: Esmo clinical practice guidelines for diagnosis, treatment and follow-up. *Annals of oncology* **25**, iii93–iii101 (2014).
2. Harpold, H. L., Alvord Jr, E. C. & Swanson, K. R. The evolution of mathematical modeling of glioma proliferation and invasion. *Journal of Neuropathology & Experimental Neurology* **66**, 1–9 (2007).
3. Jackson, P. R., Juliano, J., Hawkins-Daarud, A., Rockne, R. C. & Swanson, K. R. Patient-specific mathematical neuro-oncology: Using a simple proliferation and invasion tumor model to inform clinical practice. *BMB* **77**, 846–856 (2015).
4. Lipkova, J. *et al.* Personalized radiotherapy design for glioblastoma: Integrating mathematical tumor models, multimodal scans and bayesian inference. *IEEE Transactions on Medical Imaging* 1–1 (2019).
5. Hogue, C. *et al.* An image-driven parameter estimation problem for a reaction–diffusion glioma growth model with mass effects. *J Math Biol* **56**, 793–825 (2008).
6. Konukoglu, E. *et al.* Image guided personalization of reaction-diffusion type tumor growth models using modified anisotropic eikonal equations. *IEEE Transactions on Medical Imaging* **29**, 77–95 (2010).
7. Geremia, E. *et al.* Brain tumor cell density estimation from multi-modal mr images based on a synthetic tumor growth model. In *International MICCAI Workshop on Medical Computer Vision*, 273–282 (Springer, 2012).
8. Menze, B. *et al.* A generative approach for image-based modeling of tumor growth. In *IPMI*, 735–747 (2011).
9. Le, M. *et al.* Personalized radiotherapy planning based on a computational tumor growth model. *IEEE Transactions on Medical Imaging* **36**, 815–825 (2017).
10. Scheufe, K., Subramanian, S. & Biros, G. Automatic mri-driven model calibration for advanced brain tumor progression analysis. *arXiv: Medical Physics* (2020).
11. Subramanian, S., Scheufe, K., Himthani, N. & Biros, G. Multiatlas calibration of biophysical brain tumor growth models with mass effect. *arXiv preprint arXiv:2006.09932* (2020).
12. Hormuth, D. e. a. Image-based personalization of computational models for predicting response of high-grade glioma to chemoradiation. *Scientific Reports* **11**, 1–14 (2021).
13. Lorenzo, G. & et al. Quantitative in vivo imaging to enable tumor forecasting and treatment optimization. *arXiv preprint arXiv:2102.12602* (2021).
14. Mang, A. *et al.* Biophysical modeling of brain tumor progression: From unconditionally stable explicit time integration to an inverse problem with parabolic pde constraints for model calibration. *Medical Physics* **39**, 4444–4459 (2012).
15. Scheufe, K. *et al.* Coupling brain-tumor biophysical models and diffeomorphic image registration. *Computer methods in applied mechanics and engineering* **347**, 533–567 (2019).
16. Ezhov, I. *et al.* Geometry-aware neural solver for fast bayesian calibration of brain tumor models (2020).
17. Ezhov, I. *et al.* Neural parameters estimation for brain tumor growth modeling. In *MICCAI*, 787–795 (2019).

18. Patel, V. & Hathout, L. Image-driven modeling of the proliferation and necrosis of glioblastoma multi-forme. *Theoretical Biology and Medical Modelling* **14**, 1–9 (2017).
19. Hormuth, D. A., Eldridge, S. L., Weis, J. A., Miga, M. I. & Yankeelov, T. E. Mechanically coupled reaction-diffusion model to predict glioma growth: methodological details. In *Cancer Systems Biology*, 225–241 (Springer, 2018).
20. Pati, S. *et al.* Tmod-09. glioblastoma biophysical growth estimation using deep learning-based regression. *Neuro-Oncology* **22**, ii229–ii229 (2020).
21. Yankeelov, T. E. *et al.* Clinically relevant modeling of tumor growth and treatment response. *Science translational medicine* **5**, 187ps9–187ps9 (2013).
22. Rohlfing, T., Zahr, N. M., Sullivan, E. V. & Pfefferbaum, A. The sri24 multichannel atlas of normal adult human brain structure. *Human brain mapping* **31**, 798–819 (2010).
23. Subramanian, S., Gholami, A. & Biros, G. Simulation of glioblastoma growth using a 3d multispecies tumor model with mass effect. *Journal of mathematical biology* **79**, 941–967 (2019).
24. Lê, M. *et al.* Mri based bayesian personalization of a tumor growth model. *IEEE Transactions on Medical Imaging* **35**, 2329–2339 (2016).
25. Tunc, B., Hormuth, D., Biros, G. & Yankeelov, T. E. Modeling of glioma growth with mass effect by longitudinal magnetic resonance imaging. *IEEE Transactions on Biomedical Engineering* (2021).
26. Swanson, K. R., Alvord Jr, E. C. & Murray, J. A quantitative model for differential motility of gliomas in grey and white matter. *Cell proliferation* **33**, 317–329 (2000).
27. Subramanian, S., Scheufele, K., Mehl, M. & Biros, G. Where did the tumor start? an inverse solver with sparse localization for tumor growth models. *Inverse Problems* **36**, 045006 (2020).
28. He, K., Zhang, X., Ren, S. & Sun, J. Deep residual learning for image recognition. In *2016 IEEE Conference on Computer Vision and Pattern Recognition (CVPR)*, 770–778 (2016).
29. Menze, B. H. *et al.* The multimodal brain tumor image segmentation benchmark (brats). *IEEE transactions on medical imaging* **34**, 1993–2024 (2014).
30. Loshchilov, I. & Hutter, F. Decoupled weight decay regularization. In *International Conference on Learning Representations* (2019). URL <https://openreview.net/forum?id=Bkg6RiCqY7>.
31. Kingma, D. P. & Ba, J. Adam: A method for stochastic optimization. In *ICLR 2015* (2015).
32. Avants, B. B., Tustison, N. & Song, G. Advanced normalization tools (ants). *Insight j* **2**, 1–35 (2009).